

From Ergodicity to Many-Body Localization in a One-Dimensional Interacting Non-Hermitian Stark System

Jinghu Liu

*Institute of Theoretical Physics and State Key Laboratory of Quantum Optics
and Quantum Optics Devices, Shanxi University, Taiyuan 030006, China*

Zhihao Xu*

*Institute of Theoretical Physics and State Key Laboratory of Quantum Optics
and Quantum Optics Devices, Shanxi University, Taiyuan 030006, China and
Collaborative Innovation Center of Extreme Optics, Shanxi University, Taiyuan 030006, China*

Recent studies on disorder-induced many-body localization (MBL) in non-Hermitian quantum systems have attracted great interest. However, the non-Hermitian disorder-free MBL still needs to be clarified. We consider a one-dimensional interacting Stark model with nonreciprocal hoppings having time-reversal symmetry, the properties of which are boundary dependent. Under periodic boundary conditions (PBCs), such a model exhibits three types of phase transitions: the real-complex transition of eigenenergies, the topological phase transition, and the non-Hermitian Stark MBL transition. The real-complex and topological phase transitions occur at the same point in the thermodynamic limit, but do not coincide with the non-Hermitian Stark MBL transition, which is quite different from the non-Hermitian disordered cases. By the level statistics, the system undergoes from the Ginibre ensemble (GE) to Gaussian orthogonal ensemble (GOE) to Poisson ensemble (PE) transitions with the increase of the linear tilt potential's strength γ . The real-complex transition of the eigenvalues is accompanied by the GE-to-GOE transition in the ergodic regime. Moreover, the second transition of the level statistics corresponds to the occurrence of non-Hermitian Stark MBL. We demonstrate that the non-Hermitian Stark MBL is robust and shares many similarities with disorder-induced MBL, which several existing characteristic quantities of the spectral statistics and eigenstate properties can confirm. The dynamical evolutions of the entanglement entropy and the density imbalance can distinguish the real-complex and Stark MBL transitions. Finally, we find that our system under open boundary conditions lacks a real-complex transition, and the transition of non-Hermitian Stark MBL is the same as that under PBCs.

PACS numbers:

I. INTRODUCTION

Many-body localization (MBL) has revolutionized our understanding of quantum systems by revealing the existence of robust localized states in disordered interacting systems [1–11]. It provides an example of a quantum interacting system that results in the preservation of a non-thermal state [12–16]. Much theoretical effort was invested in its unusual features, such as the connections of MBL transitions and the random matrix theory [17, 18], the logarithmic increase in entanglement entropy with time [19, 20], the area law entanglement entropy for eigenstates [21, 22], the persistent density imbalance [23, 24], the emergent integrability [25, 26], and the response to external probes [27, 28] and periodic driving [29–31]. The experimental community has also devoted significant attention to this field, particularly since it provides pathways to implement quantum memories and quantum dynamical control [23, 32–36]. Experimental realizations of MBL have been achieved in different platforms, including ultracold atoms [32, 33], trapped ions [35], and superconducting circuits [23, 36].

The disorder is not the only mechanism to realize MBL, which can be used to localize the single-particle states [37,

38]. One has suggested that MBL may exist in a translationally invariant system, such as in a system with gauge invariance or multiple particle components [39, 40]. Recently, this issue has been approached from another way: the study of the so-called Wannier-Stark localization of a non-interacting system in a uniformly tilted lattice [41–43]. From this, the interacting systems with Wannier-Stark potentials exhibit MBL-like characteristics, named Stark MBL, which has attracted considerable theoretical and experimental focus [41–53]. On the other hand, traditional quantum mechanics is based on the postulate of Hermiticity, which assumes that Hermitian operators represent physical observables. This postulate ensures that the eigenvalues of these operators are real and the corresponding eigenvectors are orthogonal [54, 55]. However, in recent years, there has been a growing interest in exploring non-Hermitian quantum mechanics to understand and describe a wide range of physical phenomena that cannot be captured within the framework of traditional Hermitian quantum mechanics, such as the non-Hermitian skin effect (NHSE) [56, 57], the boundary-dependent spectra [58], the failure of the bulk-edge correspondence [59, 60], and the non-Bloch band theory [61–63]. Introducing the non-Hermiticity into the disorder systems has brought a new perspective on the localization features. According to the random matrix theory, the spectral statistics of non-Hermitian disorder systems display distinct features from the Hermitian ones [64–67]. The interplay between the on-site random disorder and the nonreciprocal hopping, first proposed by the pioneering works of Hatano

*Electronic address: xuzhihao@sxu.edu.cn

and Nelson, reveals a finite delocalization-localization transition accompanied by a real-complex transition of a single-particle spectrum and a topological phase transition point [68–70]. Furthermore, one can find that the random on-site potential can suppress the complex spectrum of an interacting Hatano-Nelson model with time-reversal symmetry (TRS) under periodic boundary conditions (PBCs) [71], which exhibits a coincidence of the spectral transition with the non-Hermitian MBL transition and the topological phase transition [72]. The such triple-phase transition has also been detected in TRS quasiperiodic systems under PBCs with/without interactions [73–76]. However, due to anomalous behavior under open boundary conditions (OBCs) for a non-Hermitian case that describes the localization occurring at one of the boundaries of non-Hermitian open lattices for a vast number of bulk modes, more and more studies focus on the so-called NHSE, which can be understood by applying the non-Bloch band theory. More recently, the fate of skin modes in interacting fermionic and bosonic systems and the robustness of NHSE on the localization features of many-body disordered systems have been investigated [62].

Here, we approach the question of non-Hermitian MBL without disorder from a different view by introducing interactions into a one-dimensional (1D) nonreciprocal single-particle model subjected to Wannier-Stark potentials having TRS. The so-called non-Hermitian Stark MBL is robust, exhibiting many similarities and differences with non-Hermitian disorder-induced MBL having TRS. Under PBCs, with the uniform force increase, the system's spectral statistics change from Ginibre ensemble (GE) to Gaussian orthogonal ensemble (GOE) to Poisson statistics [64–66]. The first transition corresponds to the real-complex and topological phase transitions in the thermodynamic limit. Moreover, the second transition corresponds to the non-Hermitian Stark MBL transition. Such two transitions do not coincide, which is quite different from the non-Hermitian disordered cases. In the Refs. [71–73], authors studied a non-Hermitian disordered system with a random or quasiperiodic modulated on-site potential. Under PBCs, both non-Hermitian disordered systems display the coincidence of the real-complex transition, the topological phase transition, and the MBL transition. And the corresponding statistical distribution behavior undergoes from GE to Poisson ensemble transition with the increase of the disorder amplitude. However, under OBCs, one exhibits a non-Hermitian Stark MBL with a spectral transition from GOE to Poisson statistics. We also study the similarities and differences of the non-Hermitian many-body Stark system between PBCs and OBCs by the dynamical entanglement entropy and the evolution of the density imbalance.

The rest of this paper is organized as follows. In Sec. II, we introduce a 1D nonreciprocal lattice model in the presence of a linear potential. In Sec. III, we discuss the spectral transition, the topological phase transition, the level statistics, the static entanglement entropy, the entanglement entropy with times and the quench dynamics of the density imbalance under PBCs. In Sec. IV, we study the non-Hermitian Stark MBL transition under OBCs. In Sec. V, we display the phase diagrams under PBCs and OBCs. Finally, a conclusion is given

in Sec. VI.

II. MODEL

We consider a 1D interacting Stark model with non-reciprocal hoppings having TRS, which can be described by

$$\hat{H} = J \sum_j \left(e^g \hat{c}_j^\dagger \hat{c}_{j+1} + e^{-g} \hat{c}_{j+1}^\dagger \hat{c}_j \right) + \sum_j W_j \left(\hat{n}_j - \frac{1}{2} \right) + V \sum_j \left(\hat{n}_j - \frac{1}{2} \right) \left(\hat{n}_{j+1} - \frac{1}{2} \right), \quad (1)$$

where \hat{c}_j^\dagger is the fermionic creation operator at site j and $\hat{n}_j = \hat{c}_j^\dagger \hat{c}_j$ is the associated particle-number operator, J is the nearest-neighbor hopping strengths, V is the nearest-neighbor interaction strength. One can tune the parameter g to control the non-Hermiticity of the system. To realize a non-Hermitian setup, one can continuously monitor quantum many-body systems and justify the non-Hermitian dynamics for individual quantum trajectories with no quantum jumps [55, 77–79]. We emphasize that studying the non-Hermitian treatment for a many-body Stark model is non-trivial, quite different from the Hermitian case and the master-equation approach [80]. To study the non-Hermitian Stark MBL transition, we consider the on-site potential energy can be written as [41–43]

$$W_j = -\gamma j + \alpha \left(\frac{j}{L-1} \right)^2, \quad (2)$$

where the linear tilt strength is γ , α represents the strength of the curvature, and L is the system size. We introduce a small value of α to weakly break translation invariance, so the curvature's effect is to lift the degeneracies and stabilize the localization. The factor of $1/(L-1)^2$ in Eq. (2) is required to prevent the curvature from dominating the linear part in the thermodynamic limit. For a non-interacting Hermitian case with $V = 0$ and $g = 0$, the single-particle wave functions display a Wannier-Stark localization [41–43]. In interaction, the Hermitian version occurs a Stark MBL, which has been observed in Refs. [45–48]. The MBL of the Stark model with the weak disorder has been discussed in Refs. [44, 51]. However, the non-Hermitian case is less considered.

This work focuses on the non-Hermitian interacting Stark model with the system size L at half-filling with the total particle number $N = L/2$. We apply the exact diagonalization method to study such a non-Hermitian system with the Hilbert space dimension $D = \binom{L}{L/2}$ under PBCs and OBCs, respectively. For convenience, we shall set $J = 1$ as the unit of energy and choose $V = 1$, $g = 0.1$ and $\alpha = 0.5$ for our discussion.

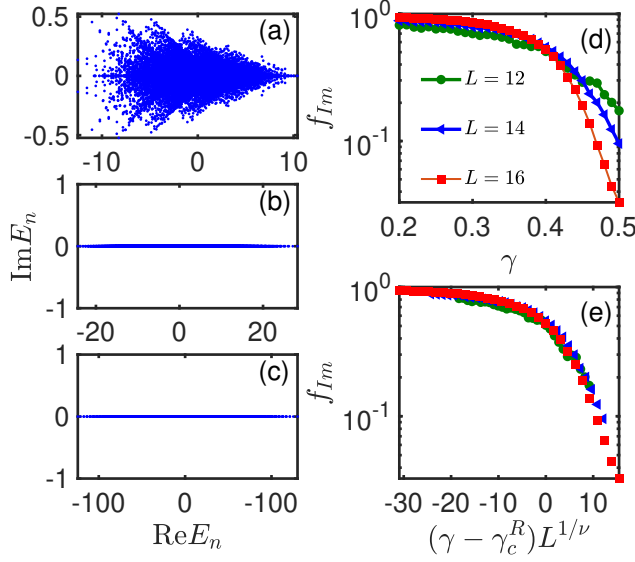


FIG. 1: (Color online) (a)-(c) The eigenvalues of the Hamiltonian (1) with $L = 16$ for $\gamma = 0.2, 0.8$, and 4 , respectively. (d) The dependence of f_{Im} on γ for different system sizes. As L increases, f_{Im} increases for $\gamma \lesssim \gamma_c^R$ (≈ 0.4), and decreases for $\gamma \gtrsim \gamma_c^R$. (e) The critical scaling collapse of f_{Im} as a function of $(\gamma - \gamma_c^R) L^{1/\nu}$ with $\gamma_c^R = 0.4$ and $\nu = 0.55$. Here, we choose PBCs.

III. INTERACTING NON-HERMITIAN STARK MODEL UNDER PERIODIC BOUNDARY CONDITIONS

A. Real-complex transition of eigenvalues

We first consider the spectral transition of the Hamiltonian (1). Figures 1(a)-1(c) show the eigenvalues of the Hamiltonian (1) with $L = 16$ under PBCs for $\gamma = 0.2, 0.8$, and 4 , respectively. Due to the TRS, the energy spectrum is symmetric around the real axis. With the uniform force γ increase, the eigenvalues with nonzero imaginary parts decrease. To quantitatively investigate the fraction of the complex eigenvalues, we define $f_{\text{Im}} = D_{\text{Im}}/D$ with a cut-off $C = 10^{-13}$ [71, 73, 81]. When $|\text{Im} E| \leq C$, it is identified as a machine error. Here, D_{Im} is the number of the eigenvalues with nonzero imaginary parts. As shown in Fig. 1(d), we show f_{Im} as a function of γ for different system sizes L . As L increases, f_{Im} increases for $\gamma \leq \gamma_c^R \approx 0.4$, and decreases for $\gamma \geq \gamma_c^R$. We further perform the finite-size scaling collapse of f_{Im} by employing the ansatz $(\gamma - \gamma_c^R) L^{1/\nu}$ [Fig. 1(e)], indicating a real-complex transition of many-body eigenvalues at $\gamma = \gamma_c^R$ with $\nu \approx 0.55$ in the thermodynamic limit. That means in the thermodynamic limit, almost all the eigenvalues are complex when $\gamma < \gamma_c^R$, and for $\gamma > \gamma_c^R$, the eigenvalues turn to real numbers. Similar results are found in a non-Hermitian many-body system with random or quasiperiodic on-site potentials. However, our model displays different scaling exponent ν from ones in random and quasiperiodic systems, which indicates that the real-complex transition of

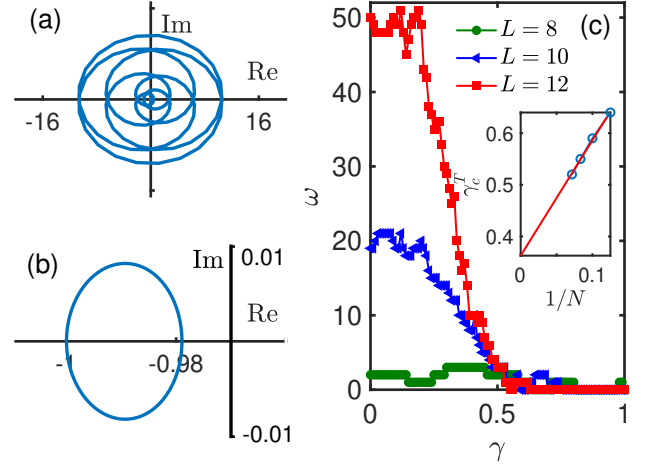


FIG. 2: (Color online) The dependence of $\det[H(\Phi)]/\det[H(0)]$ in the complex plane with $L = 10$ for (a) $\gamma = 0.4$ and (b) 1.0 . (c) The winding number ω as a function of γ with $L = 8, 10, 12$. Inset: The topological phase transition γ_c^T as function of size $1/N$.

the interacting non-Hermitian Stark model is in different universality classes from the disordered cases.

B. Topological phase transition

Unlike the Hermitian cases, our interacting non-Hermitian Stark system displays a topological phase transition in the complex energy plane [73, 74, 82]. We introduce the winding number ω to characterize the topological feature of our system, which is given as follows [73, 74]:

$$\omega = \int_0^{2\pi} \frac{d\Phi}{2\pi i} \partial_\Phi \ln \det[H(\Phi) - E_B], \quad (3)$$

where $H(\Phi)$ is the Hamiltonian (1) under PBCs, the phase Φ is a magnetic flux penetrating through the center of the ring chain, and E_B is a basis energy. The winding number ω counts times of the complex spectral trajectory encircling the chosen basis energy E_B when the phase Φ rolls from 0 to 2π . One has demonstrated that the winding number does not depend on the choice of E_B [83]. In this case, we choose $E_B = 0$. Since it is hard to directly apply Eq. (3) for the many-body systems, we alternatively use the Φ -dependence of $\det[H(\Phi)]/\det[H(0)]$ to calculate the number of the loop winding around E_B , which is equal to the winding number [83]. Figures 2(a) and 2(b) show $\det[H(\Phi)]/\det[H(0)]$ in the complex plane with the rolling of the phase Φ from 0 to 2π with $L = 10$ for $\gamma = 0.4$ and 1 , respectively. In Fig. 2(a), we find that $\det[H(\Phi)]/\det[H(0)]$ draws a close loop around $E_B = 0$ eight times, which corresponds to $\omega = 8$. In contrast, $\det[H(\Phi)]/\det[H(0)]$ for $\gamma = 1$ and $L = 10$ in Fig. 2(b) shows a close curve without surrounding $E_B = 0$, corresponding to a topologically trivial case. Figure 2(c) shows the winding number ω as a function of γ with different L . According to Fig. 2(c), one can see that ω decreases with the

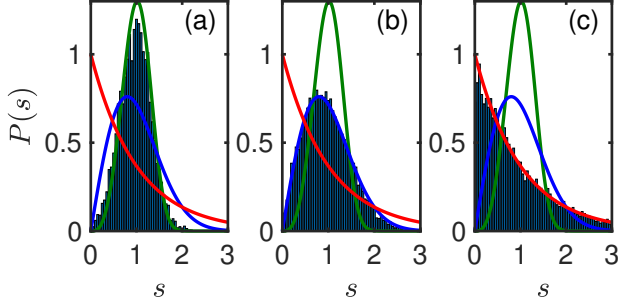


FIG. 3: (Color online) (a)-(c) The unfolded nearest-level-spacing distribution of the Hamiltonian (1) with $L = 16$ for $\gamma = 0.2, 0.8$, and 4 , respectively. The green, blue, and red lines represent the Ginibre, GOE, and Poisson distributions, respectively. Here, we choose PBCs.

increase of γ and the system size L , unlike the single-particle Hermitian cases only with the nearest-neighbor hoppings that the winding number is found as $\omega = \pm 1$ for the topologically nontrivial phase. It implies that the non-Hermitian many-body systems exhibit much more complicated topological structures. On the other hand, the curves in Fig. 2(c) show that the transition from a topologically nontrivial phase with $\omega > 0$ to a trivial one with $\omega = 0$ around at $0.64, 0.59$, and 0.55 for $L = 8, 10$, and 12 , respectively. Note that the topological phase transition does not equal the real-complex transition in finite-size cases. However, complex eigenvalues are necessary to construct the close loops in the energy plane. The winding number defined in the complex plane by the gauge transformation is a collective indicator of eigenvalues being complex or real of the original Hamiltonian. The slight difference between the γ_c^R and γ_c^T can be ascribed to the finite-size effect. A finite-size scaling of γ_c^T with $1/N$ is shown in the inset of Fig. 2(c). In the thermodynamic limit, the topological phase transition converges to finite value $\gamma_c^T = 0.36 \pm 0.04$ (the error represents the 95% confidence interval), which is close to the real-complex transition point. Hence, we can conjecture that both transition points should coincide in the thermodynamic limit.

C. Non-Hermitian Stark many-body localization

We next study an ergodicity-to-MBL transition in the interacting non-Hermitian Stark system. The level statistics is a powerful tool to diagnose the emergence of non-Hermitian MBL. In the conventional non-Hermitian disorder systems with TRS, the ergodic phase follows the GE, and the MBL phase follows the real Poisson ensemble. We first consider the nearest-level spacing distribution of unfolded eigenenergies in the complex plane [17, 71]. Here, the nearest-level-spacings for a given eigenvalue E_n (before unfolding) are defined as $d_{1,n} = \min_m |E_n - E_m|$ in the complex energy plane, which is non-universal and system-dependent. In order to compare theoretical predictions of random matrix theory with actually

computed level sequences, one should perform an unfolding procedure. After a standard unfolding procedure, one can obtain the normalized level spacing s with $\int_0^\infty p(s)ds = 1$. And the unfolding nearest-level-spacings $s_n = d_{1,n}\sqrt{\bar{\rho}_n}$, where $\bar{\rho}_n = \tilde{n}/(\pi d_{\tilde{n},n}^2)$ is the local mean density, \tilde{n} is sufficient large than unit, i.e., $\tilde{n} \approx 30$, and $d_{\tilde{n},n}$ is the \tilde{n} th nearest-neighbor distance from E_n .

For a small uniform force, the complex energy spectrum obeys the GE distribution $P_{\text{GE}}(s) = cp(cs)$ shown in Fig. 3(a) with $\gamma = 0.2$, where [71]

$$p(s) = \lim_{N \rightarrow \infty} \left[\prod_{n=1}^{N-1} e_n(s^2) e^{-s^2} \right] \sum_{n=1}^{N-1} \frac{2s^{2n+1}}{n!e_n(s^2)}, \quad (4)$$

with $e_n(x) = \sum_{m=0}^n \frac{x^m}{m!}$ and $c = \int_0^\infty sp(s)ds = 1.1429$, which matches with the non-Hermitian random matrices in AI class symmetry class. We further increase γ beyond γ_c^R , the system's spectrum exhibits a real-complex transition, where the real eigenspectrum of a weak uniform force case follows the level statistics of GOE. The level-spacing distribution of GOE is [71]

$$P_{\text{GOE}}(s) = \frac{\pi s}{2} e^{-\pi s^2/4}. \quad (5)$$

As shown in Fig. 3(b) with $\gamma = 0.8 > \gamma_c^R$, the near-neighbor level spacing distribution becomes a GOE case. For large enough γ , the system immerses into the MBL phase with the real eigenspectrum, which is characterized by the real Poisson level distribution [71]

$$P_{\text{Pois}}(s) = e^{-s}. \quad (6)$$

We take $\gamma = 4$ as an example [Fig. 3(c)], the real eigenspectrum distribution becomes the Poissonian. These results demonstrate that the non-Hermitian Stark system also has an MBL phase transition with the increase of γ . However, in the ergodic regime, the system undergoes a real-complex transition of eigenvalues, which leads to the nearest-neighbor level spacing distribution from the GE distribution to the GOE distribution.

We further consider the complex spacing ratio (CSR) for the n th eigenvalue is defined as the ratio of complex differences given by [65]

$$\xi_n = \frac{E_n - E_n^{\text{NN}}}{E_n - E_n^{\text{NNN}}} = r_n e^{i\theta_n}, \quad (7)$$

where E_n^{NN} and E_n^{NNN} are the nearest- and the next-nearest-neighbor of the energy level E_n in the complex plane, respectively. Note that r_n and θ_n are the magnitude and the argument of the complex ratio ξ_n . The nearest-neighbor difference is non-universal and depends on the local density of states. In contrast, in the ratio ξ_n , the local density of state's information is washed away. Hence, the CSR is a preferable diagnostic to detect an ergodicity-to-MBL transition. According to the definition of CSR, $r_n \in [0, 1]$ and $\theta \in (-\pi, \pi] \forall n$. We focus on the radial and angular marginal distributions, denoted by $\varrho(r)$ and $\varrho(\theta)$, respectively. Both distributions $\varrho(r)$ and $\varrho(\theta)$ have

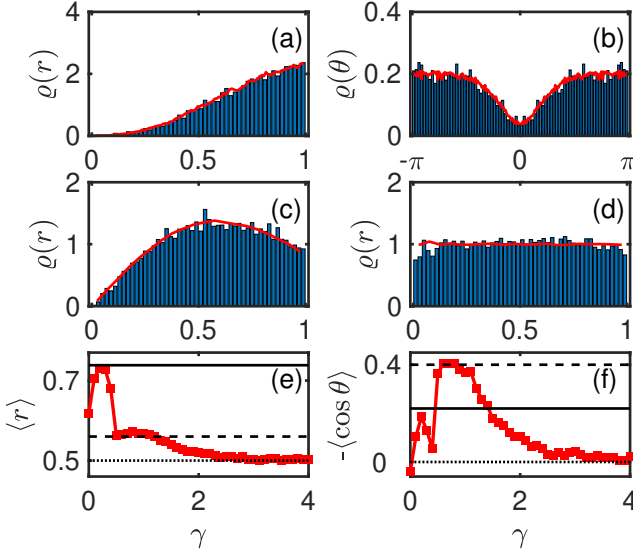


FIG. 4: (Color online) (a)-(b) The marginal distributions $\rho(r)$ and $\rho(\theta)$ with $\gamma = 0.2$ for the complex energy spectrum. (c)-(d) The distributions $\rho(r)$, respectively, with $\gamma = 0.8$ and 4 for the real energy spectrum. The solid red lines are obtained by calculating $\rho(r)$ and $\rho(\theta)$ of the 200×200 symmetric random matrices with the corresponding random matrix ensembles averaged 1000 realizations. (e) The average magnitude $\langle r \rangle$ as a function of γ . The solid, dashed, and dotted lines represent $\langle r \rangle = 0.74$, 0.56 , and 0.5 , respectively. (f) $-\langle \cos \theta \rangle$ as a function of γ . The solid, dashed, and dotted lines denote $-\langle \cos \theta \rangle = 0.22$, 0.4 , and 0 , respectively. Here, we choose PBCs and $L = 16$.

distinct features for different random matrix ensembles. Figure 4 shows $\rho(r)$ and $\rho(\theta)$ for different γ with $L = 16$. For $\gamma = 0.2$, the complex-valued spectrum of our system follows a GE distribution, in which the spectrum experience level repulsion with the vanishing of $\rho(r)$ for small r [Fig. 4(a)], and $\rho(\theta)$ display a non-uniformity [Fig. 4(b)]. When $\gamma > \gamma_c^R$, the eigenvalues become real, and the angular marginal distribution $\rho(\theta)$ collapses to $\theta = 0$ and π . When the system is localized at the ergodic regime following the GOE, $\rho(r)$ displays similar behavior to that following the GE [see Fig. 4(c) with $\gamma = 0.8$]. In Fig. 4(d) with $\gamma = 4$, the system immerses into the MBL phase with an uncorrelated energy level, and the corresponding $\rho(r)$ is flat. The solid red lines shown in Fig. 4 are obtained by calculating $\rho(r)$ and $\rho(\theta)$ of the 200×200 symmetric random matrices with the corresponding random matrix ensembles averaged 1000 realizations, which are fit well with the interaction non-Hermitian Stark model. By detecting the average $\langle r \rangle$ and $-\langle \cos \theta \rangle$, one can obtain the phase transition information, where $\langle r \rangle = \int_0^1 dr r \rho(r)$ and $-\langle \cos \theta \rangle = -\int_{-\pi}^{\pi} d\theta \cos \theta \rho(\theta)$. We first consider $\langle r \rangle$ as a function of γ shown in Fig. 4(e) with $L = 16$. For a small γ ($\gamma < \gamma_c^R$), the $\langle r \rangle$ attains a constant value ≈ 0.74 for the GE distribution [65, 81, 84, 85]. When γ is chosen as an intermediate value, Fig. 4(e) shows a transition to $\langle r \rangle \approx 0.56$, corresponding to the GOE [81, 85]. Such transition is consistent

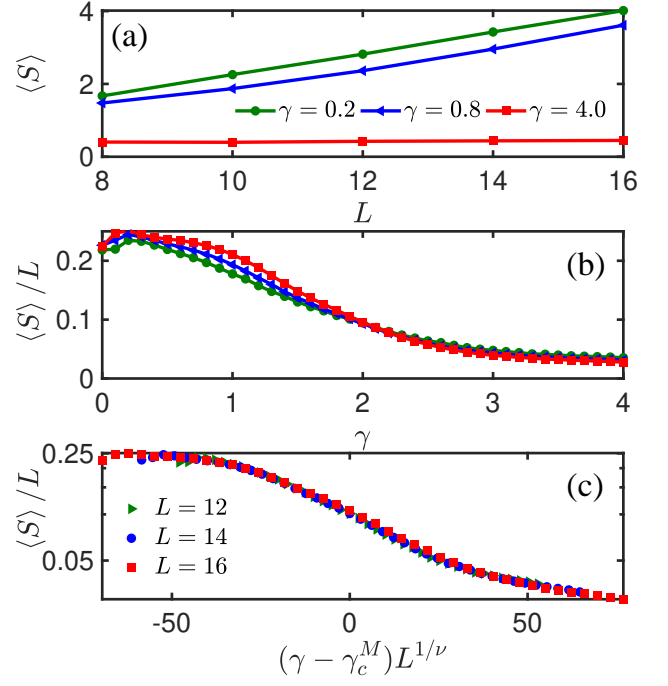


FIG. 5: (Color online) (a) The averaged half-chain entanglement entropy $\langle S \rangle$ as the function of L for different γ . (b) $\langle S \rangle / L$ as the function of γ for different L . (c) The critical scaling collapse of $\langle S \rangle / L$ as a function of $(\gamma - \gamma_c^M) L^{1/\mu}$ with $\gamma_c^M \approx 1.9$ and $\mu \approx 0.77$. Here, we choose PBCs.

with the corresponding spectral transition. When γ increase to the strong tilt limit, the system undergoes the γ -induced Stark MBL transition accompanied by a change in $\langle r \rangle$ from GOE to real Poisson statistics. For a real Poisson statistic, the non-Hermitian system has $\langle r \rangle \approx 0.5$ [81, 85]. Likewise, the single number signature of $-\langle \cos \theta \rangle$ can also distinguish the different phase regimes with different level distributions. For the system with the GE distribution $-\langle \cos \theta \rangle \approx 0.22$ [65, 81, 84], which is shown in Fig. 4(f) with $-\langle \cos \theta \rangle$ as the function of γ . As γ increases, we find a dip in $-\langle \cos \theta \rangle$, which can demarcate the complex and real energy phases. In the GOE regime, $-\langle \cos \theta \rangle$ approaches a finite value about 0.4. Though the spectrum is real in this case, the real CRS $\xi_n \in [-1, 1]$ with the argument of ξ_n being $\theta = 0$ or π . We find that ξ_n with the negative values are more than positive values. By statistics, $-\langle \cos \theta \rangle$ approaches 0.4 in the GOE regime. When the system goes into the Stark MBL phase with the Poisson statistics, $-\langle \cos \theta \rangle = 0$. The main features of $-\langle \cos \theta \rangle$ agree with the behavior of $\langle r \rangle$. Notice that when $\gamma \rightarrow 0$, the values of $\langle r \rangle$ and $-\langle \cos \theta \rangle$ display a distinct deviation from the standard values in the GE regime. Observing the on-site potential Eq. (2), we find that in the $\gamma \rightarrow 0$ limit, the quadratic term predominates. In the small γ limit, the symmetry axis of the potential function $j_o = \gamma(L-1)^2/(2\alpha) \in [0, L-1]$, which leads to the increase of the energy degeneracy and the deviation of the corresponding $\langle r \rangle$ and $-\langle \cos \theta \rangle$. To avoid the deviation, one can choose a larger $\gamma \geq 2\alpha/(L-1)$ for

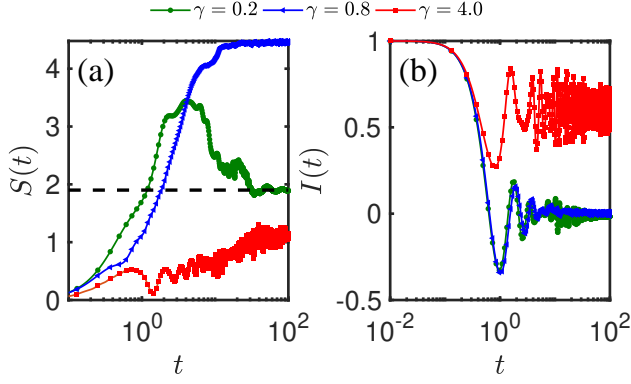


FIG. 6: (Color online) (a) Dynamics of the half-chain entanglement entropy $S(t)$ for different γ . (b) The dynamical evolution of the density imbalance $I(t)$ for different γ . Here, $L = 16$ under PBCs, and the initial state is set as $|\psi_0\rangle = |0101 \dots\rangle$.

discussion (see Appendix A for details).

We use the static half-chain entanglement entropy $S_n = -\text{Tr}[\rho_{L/2}^n \ln \rho_{L/2}^n]$ to exact obtain the non-Hermitian Stark MBL transition point. Here, $\rho_{L/2}^n = \text{Tr}_{L/2}[|E_n^r\rangle\langle E_n^r|]$, where $|E_n^r\rangle$ is normalized right eigenstates, i.e., $\langle E_n^r | E_n^r \rangle = 1$, and $\rho_{L/2}^n$ is the half-chain reduced density matrix obtained by tracing out half of the system. In Fig. 5(a), we display the average entanglement entropy $\langle S \rangle$ averaged over all the right eigenstates as a function of L with different γ . From Fig. 5(a) for $\gamma = 0.2$ and 0.8 , one can see that $\langle S \rangle$ follows a volume law in the ergodic phase. However, it decreases to a constant independent of L in the deep MBL phase with $\gamma = 4$, which fulfills an area law. Figure 5(b) shows the L -dependence of $\langle S \rangle / L$ as a function of γ . In Fig. 5(b), one can see that the average entanglement entropy $\langle S \rangle / L$ exhibits a crossover from the volume to area law as the non-Hermitian Stark MBL phase sets in around $\gamma_c^M \approx 1.9$. We confirm the critical scaling collapse as a function of $(\gamma - \gamma_c^M)L^{1/\mu}$, which is shown in Fig. 5(c) with $\mu = 0.7$. These results show that the ergodic and stark MBL phases can be distinguished by entanglement entropy, even in non-Hermitian systems, like the Hermitian cases.

According to our numerical calculation, there are three kinds of phase transitions: the real-complex transition of eigenvalues, the topological phase transition, and the non-Hermitian Stark MBL transition. The corresponding transition points γ_c^R and γ_c^T coincide in the thermodynamic limit but do not coincide with γ_c^M , which differs from the non-Hermitian cases with disordered on-site potentials.

D. Dynamical features

In this subsection, we discuss the nonequilibrium time evolution of the non-Hermitian Stark system from the perspective of quantum trajectories without jump conditions for the continuously monitored system. We choose a given initial state

$|\psi_0\rangle = |0101 \dots\rangle$ at $t = 0$, the dynamical evolution can be encoded in the wave function $|\psi_t\rangle = e^{-i\hat{H}t}|\psi_0\rangle/\sqrt{\mathcal{N}}$ with the normalized coefficient $\mathcal{N} = \langle\psi_0|e^{iH^\dagger t}e^{-iHt}|\psi_0\rangle$. With the help of the time-dependent wave function, many dynamical features can be detected.

The dynamics of a half-chain entanglement entropy can be defined as [86]

$$S(t) = -\text{Tr}[\rho_{L/2}(t) \ln \rho_{L/2}(t)], \quad (8)$$

where $\rho_{L/2}(t) = \text{Tr}_{L/2}[|\psi_t\rangle\langle\psi_t|]$ is the reduced density matrix of $|\psi_t\rangle$. The time evolution of $S(t)$ for different γ with $L = 16$ is shown in Fig. 6(a). For $\gamma = 4$, the evolution of $S(t)$ displays a logarithmic growth, which characterizes the Stark MBL. For $\gamma = 0.2$ and 0.8 cases, the short-time evolution of $S(t)$ shows a linear growth. However, $S(t)$ can decrease after $t \approx 10$ in the complex eigenvalue phase ($\gamma = 0.2$) but remain a stable value in the real eigenenergy phase ($\gamma = 0.8$). The results of the dynamical evolution of $S(t)$ imply that one can detect the occurrence of the Stark MBL by the short-time evolution of $S(t)$, and the long-time behavior of $S(t)$ signifies the real-complex transition.

We further investigate the dynamics of density imbalance for different γ , which is defined as [23, 24, 81]

$$I(t) = \frac{N_e(t) - N_o(t)}{N_e(t) + N_o(t)}, \quad (9)$$

where $N_e(t) = \sum_{\tilde{j}} \langle\psi_t|\hat{n}_{2\tilde{j}}|\psi_t\rangle$ and $N_o(t) = \sum_{\tilde{j}} \langle\psi_t|\hat{n}_{2\tilde{j}+1}|\psi_t\rangle$ with \tilde{j} being an integer. Figure 6(b) shows the dynamics of density imbalance $I(t)$ for different γ . In the ergodic phase, $I(t)$ relaxes to zero as time evolves, losing the memory of the initial information. For a large γ , $I(t)$ remains nonzero values at long times, which indicates that the system is localized in the Stark MBL phase.

IV. NON-HERMITIAN STARK MANY-BODY LOCALIZATION UNDER OPEN BOUNDARY CONDITIONS

The existence of real spectrum under OBC can be explained using an imaginary gauge transformation. Under OBCs, the nonreciprocal many-body Stark model having TRS can be mapped to a Hermitian model

$$\begin{aligned} \hat{H} = & J \sum_j \left(\hat{c}_j^\dagger \hat{c}_{j+1} + \hat{c}_{j+1}^\dagger \hat{c}_j \right) + \sum_j W_j \left(\hat{n}_j - \frac{1}{2} \right) \\ & + V \sum_j \left(\hat{n}_j - \frac{1}{2} \right) \left(\hat{n}_{j+1} - \frac{1}{2} \right), \end{aligned} \quad (10)$$

by using a gauge transformation [87], that is $\hat{c}_j \rightarrow e^{-gj} \hat{c}_j$ and $\hat{c}_j^\dagger \rightarrow e^{gj} \hat{c}_j^\dagger$. Hence, under OBCs, the spectrum of the Hamiltonian (1) is always real, and the real-complex transition of eigenvalues vanishes. In this section, we mainly discuss the Stark MBL transition under OBCs.

A well-established signature for the transition from ergodic to MBL phases is the level statistics of the spectrum. For our

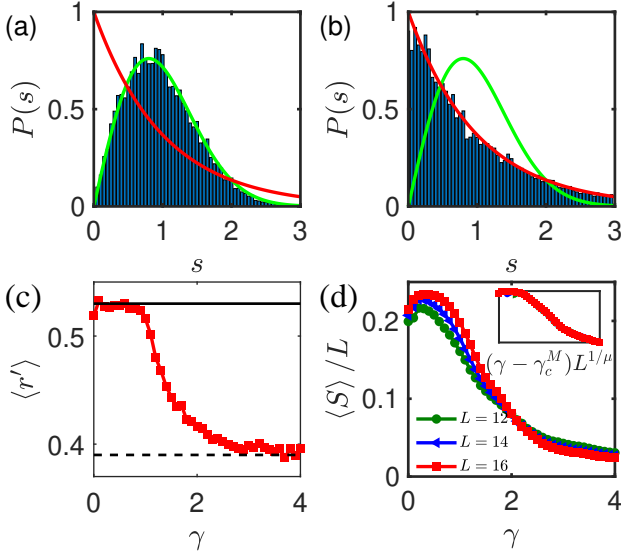


FIG. 7: (Color online) The unfolded nearest-level-spacing distribution of the Hamiltonian (1) with $L = 16$ for (a) $\gamma = 0.2$ and (b) $\gamma = 4$. The green and red lines represent the GOE and Poisson distributions. (c) The average ratio of adjacent energy gaps $\langle r' \rangle$ as a function of γ with $L = 16$. The solid and dashed lines corresponds to the GOE and Poisson predictions, respectively. (d) $\langle S \rangle / L$ as the function of γ for different L . Inset: The critical scaling collapse of $\langle S \rangle / L$ as a function of $(\gamma - \gamma_c^M) L^{-1/\mu}$ with $\gamma_c^M \approx 1.9$ and $\mu \approx 0.77$. Here, we choose OBCs.

model under OBCs with the real spectrum in the delocalized and ergodic phase, one expects the GOE of random matrix theory to be relevant. In contrast, the MBL phase with a real spectrum will lead to real Poisson-level statistics. We perform a standard unfolding procedure of the real energy spectrum, obtaining level sequences of unit mean spacing. Figures 7(a) and 7(b) show the nearest-level spacing distribution $P(s)$ of unfolded eigenvalues under OBCs with $L = 16$ for $\gamma = 0.2$ and 4, respectively. For $\gamma = 0.2$, $P(s)$ fits the GOE distribution described by Eq. (5). However, when the system is localized in the MBL phase, the nearest-level spacing distribution follows the real Poisson distribution as Eq. (6) shown in Fig. 7(b) with $\gamma = 4$. A simple indicator for a real spectrum to detect the MBL transition is the average ratio $\langle r' \rangle$ between the smallest and the largest adjacent energy gaps given by [18]

$$\langle r' \rangle = \frac{\min\{\delta_n^E, \delta_{n-1}^E\}}{\max\{\delta_n^E, \delta_{n-1}^E\}}, \quad (11)$$

with $\delta_n^E = E_n - E_{n-1}$, and E_n is ordered in ascending order. In the ergodic (MBL) phase, $\langle r' \rangle$ is close to the GOE value $\langle r' \rangle \approx 0.53$ (the Poisson value $\langle r' \rangle \approx 0.38$). As shown in Fig. 7(c), we can see that $\langle r' \rangle$ exhibits a clear transition from 0.53 to 0.38 with the increase of γ , which indicates the non-Hermitian Stark MBL also emerges under OBCs.

We further determine the Stark MBL phase transition by the static half-chain entanglement entropy under OBCs. Figure 7(d) shows the system-size dependence of $\langle S \rangle / L$ averaged

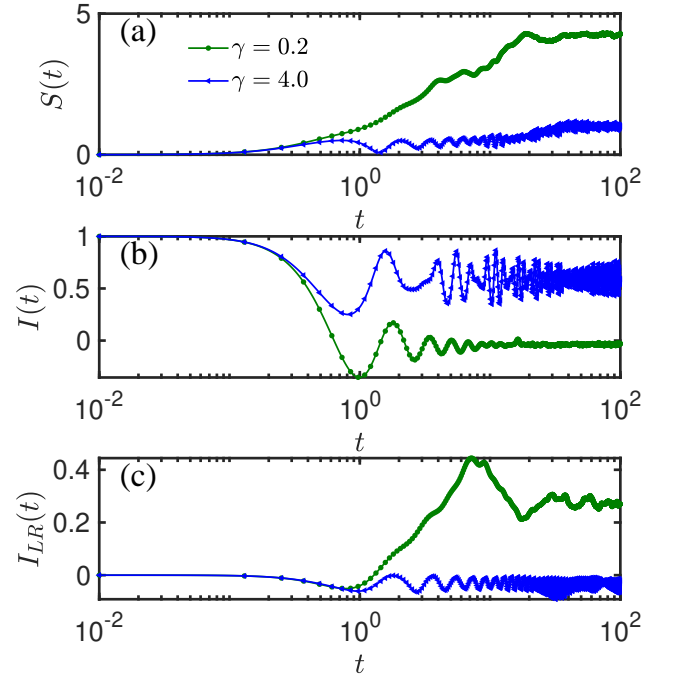


FIG. 8: (Color online) (a) Dynamics of the half-chain entanglement entropy $S(t)$ for different γ . (b) The dynamical evolution of the density imbalance $I(t)$ for different γ . (c) Dynamics of the left-right imbalance $I_{LR}(t)$ for different γ . Here, $L = 16$ under OBCs, and the initial state is set as $|\psi_0\rangle = |0101 \dots\rangle$.

over all the eigenstates for different L as a function of γ under OBCs. The static half-chain entanglement entropy exhibits a crossover from the volume to area law. We perform a finite-size critical collapse for $\langle S \rangle / L$ shown in the inset of Fig. 7(d). Our numerical results show that $\gamma_c^M \approx 1.9$ and $\mu \approx 0.77$ under OBCs are the same as those under PBCs.

In Fig. 8(a), we show the results for the dynamics of half-chain entanglement entropy $S(t)$ with the initial state $|0101 \dots\rangle$ under OBCs. For $\gamma > \gamma_c^M$ ($\gamma = 4.0$), $S(t)$ grows as a logarithmic behavior and remains low values in the long-time limit indicating the emergence of Stark MBL. For $\gamma = 0.2$, the short-time evolution of $S(t)$ shows a linear growth. Unlike the PBC case, $S(t)$ remains a stable value without the emergence of decreasing, which indicates that the spectrum of the system in the small γ case is real.

The NHSE is an iconic phenomenon, which exhibits the localization of a large number of eigenstates at the boundaries under OBCs. To distinguish the Stark MBL from the NHSE, we can utilize the dynamical evolution of the density imbalance $I(t)$ and the left-right imbalance [88]

$$I_{LR}(t) = \sum_{j \leq L/2} \langle \hat{n}_j(t) \rangle - \sum_{j > L/2} \langle \hat{n}_j(t) \rangle \quad (12)$$

with the even L shown in Figs. 8(b) and 8(c), respectively. Here, we choose the initial state $|0101 \dots\rangle$. When the system is localized in the ergodic phase $\gamma < \gamma_c^M$ exhibiting the NHSE, $I(t)$ decays quickly with t , and in the long time limit,

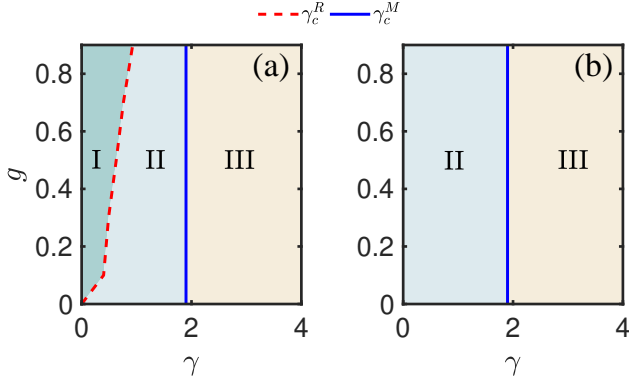


FIG. 9: (Color online) (a) Phase diagram for the non-Hermitian Stark model under PBCs, which contains three phases: Phase I (the complex ergodic phase), Phase II (the real ergodic phase) and Phase III (the Stark MBL phase). The phase transition positions γ_c^R and γ_c^M are marked by the dashed and solid lines, respectively. (b) Phase diagram for the non-Hermitian Stark model under OBCs.

$I(t) \rightarrow 0$ and $I_{LR}(t)$ is finite. However, for $\gamma = 4.0$ shown in Fig. 8(b), $I(t)$ displays a decay in the short time, and $I(t)$ stays finite and I_{LR} tends to zero in the long time limit, which indicate that the system is localized in the Stark MBL phase without exhibiting the NHSE.

V. PHASE DIAGRAMS

In this section, we observe the phase diagrams of Hamiltonian (1) on the g - γ plane under PBCs and OBCs, as illustrated in Figs. 9(a) and 9(b), respectively. As seen in Fig. 9(a), there are three phases in this system under PBCs: Phase I, Phase II, and Phase III corresponding to the ergodic regime with the GE distribution, the ergodic regime with the GOE distribution, and the Stark MBL regime with the Poisson statistics. The phase transition positions γ_c^R and γ_c^M are marked by the dashed and solid lines, respectively. As g increases, the regime with the complex spectrum enlarges. However, the transition of the Stark MBL is not sensitive to g . Under OBCs shown in Fig. 9(b), there are two phases in the phase diagram due to the real spectrum for the whole parameter region. The Stark MBL transition points seem g insensitive, *i.e.*, $\gamma_c^M \approx 1.9 \pm 0.1$, which is marked by the solid line in Fig. 9(b).

VI. CONCLUSIONS

In this paper, we first discussed the real-complex transition, topological phase transition, and Stark MBL phase transition in an interacting non-Hermitian Stark model having TRS under PBCs. Unlike the non-Hermitian disordered cases with the random or quasiperiodic modulated on-site potential displaying the coincidence of such three transitions, our numerical results show that these three types of phase transition do not coincide. The level statistics show that the statistics change from

the GE to GOE to Poisson ensemble under PBCs. The first transition corresponds to a spectral transition and the topological phase transition in the thermodynamic limit. Moreover, the second transition corresponds to an ergodicity-to-MBL transition. We also demonstrate that the non-Hermitian Stark MBL is robust and similar to disorder-induced MBL. The quench dynamics can corroborate the signature of the real-complex transition and the non-Hermitian Stark MBL. Finally, we study the non-Hermitian Stark MBL under OBCs. Due to the real energy spectrum under OBCs, there is only one transition for the level statistics from GOE to Poisson ensemble, corresponding to the occurrence of non-Hermitian Stark MBL at $\gamma_c^M \approx 1.9$ the same as the case under PBCs.

The non-Hermitian systems with the tunable nonreciprocal quantum transport have been realized in ultracold atoms using the dissipative Aharonov-Bohm rings in Refs. [89, 90], which has potential application in our non-Hermitian Stark model. By detecting the time-dependent atom population of each site, one can realize the measurement of the particle population over time in the non-Hermitian Stark model, allowing us to distinguish the NHSE and the Stark MBL by the dynamical quantities $I(t)$ and $I_{LR}(t)$ presented in our paper. Besides relying on measuring dynamical quantities, analyzing the statistics of the energy spectrum is also a way to determine the Stark MBL. Fortunately, in a superconducting circuit, the many-body spectroscopy technique can retrieve the many-body eigenenergies and thereby obtain information on the level statistics of the Hamiltonian [16, 36]. However, measuring energy spectra in non-Hermitian systems is challenging due to the complex energy levels. Further developments in energy spectrum measurement techniques are needed in these cases.

Note added: on submission of this manuscript, we notice a very recent preprint arXiv:2305.09387 entitled “Non-Hermitian Stark Many-Body Localization” [91]. The authors studied a similar problem, and the main results of the emergence of the non-Hermitian Stark MBL were obtained. This paper emphasizes that the real-complex transition, the topological transition point, and the MBL transition are not identical in the interacting non-Hermitian Stark system under PBCs. However, we show the occurrence of the non-Hermitian Stark MBL without a real-complex transition in the energy spectrum under OBCs.

Acknowledgments

Z.X. is supported by the NSFC (Grants No. 12375016), the Fundamental Research Program of Shanxi Province, China (Grant No. 20210302123442), and the Open Project of Beijing National Laboratory for Condensed Matter Physics. This work is also supported by NSF for Shanxi Province Grant No. 1331KSC.

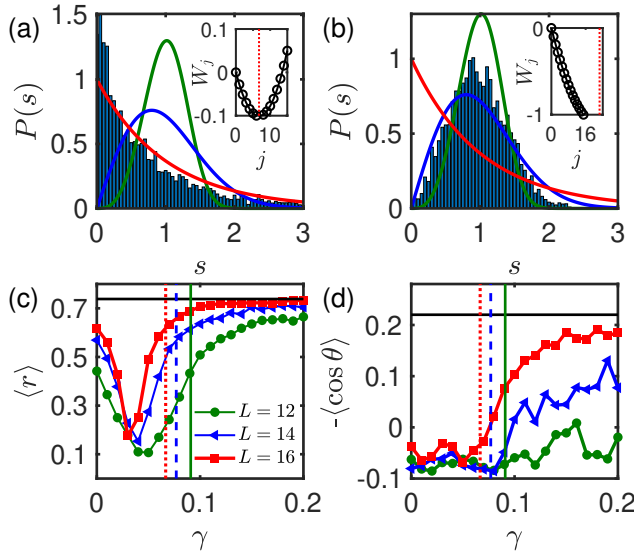


FIG. 10: (Color online) The unfolded nearest-level-spacing distribution of the Hamiltonian (1) with $L = 16$ for (a) $\gamma = 0.03$ and (b) $\gamma = 0.1$. The green, blue and red lines represent the Ginibre, GOE and Poisson distributions, respectively. Inset: The on-site potential as a function of the lattice site. The vertical dotted line indicates the symmetry axis j_o . (c) $\langle r \rangle$ as a function of γ . The horizontal solid line represent $\langle r \rangle = 0.74$. (d) $-\langle \cos \theta \rangle$ as a function of γ . The horizontal solid line denotes $-\langle \cos \theta \rangle = 0.22$. The vertical solid, dashed, and dotted lines indicate γ_s with $L = 12, 14$, and 16 , respectively. Here, we choose PBCs.

Appendix A: Spectrum statistics for $\gamma \rightarrow 0$

In the main text, Figs. 4(e) and 4(f) show a distinct deviation from the standard values in the GE case for $\gamma \rightarrow 0$. The on-site potential Eq. (2) dispalys a parabolic form. In the small γ limit, the quadratic part is predominant. One can find that there exists a symmetry axis $j_o = \gamma(L-1)^2/(2\alpha)$ seen in the insets of Figs. 10(a) and 10(b), which may induce the energy degeneracy. Figures 10(a) and 10(b) show the unfolded nearest-level-spacing distribution of the Hamiltonian (1) with $L = 16$ for $\gamma = 0.03$ and $\gamma = 0.1$, respectively. When $j_o \in [0, L-1]$, the corresponding level statistics show a Poisson-like distribution [see Fig. 10(a)], where a peak emerges at $s \rightarrow 0$ indicating the existence of high degeneracy. When $j_o > L-1$, the level statistics restore the GE distribution [see Fig. 10(b)], and the corresponding degeneracy breaks. To avoid the effect of the quadratic part, one can consider a larger γ , satisfying the condition: $\gamma \geq \gamma_s = 2\alpha/(L-1)$, which can ensure the monotonicity of the on-site potential with the lattice site. To further verify the system size-dependent condition, we plot $\langle r \rangle$ and $-\langle \cos \theta \rangle$ as a function of γ for different L in Figs. 10(c) and 10(d), respectively. The different vertical lines correspond to γ_s for different L . We can see that when $\gamma > \gamma_s$, $\langle r \rangle$ and $-\langle \cos \theta \rangle$ tend to the corresponding standard values of the GE distribution. Hence, for the small γ case, the deviation of the level statistics comes from the energy degeneracy. To avoid the deviation, one can consider the system size-dependent condition $\gamma > \gamma_s$ for the calculation.

-
- [1] D. Basko, I. Aleiner, B. Altshuler, On the problem of many-body localization, *Ann. Phys.* **321**, 1126 (2006).
 - [2] C.R. Laumann, A. Pal, A. Scardicchio, Many-body mobility edge in a mean-field quantum spin glass, *Phys. Rev. Lett.* **113**, 200405 (2014).
 - [3] R. Nandkishore, D.A. Huse, Many-body localization and thermalization in quantum statistical mechanics, *Annu. Rev. Condens. Matter Phys.* **6**, 15 (2015).
 - [4] J.A. Käll, J.H. Bardarson, F. Pollmann, Many-body localization in a disordered quantum Ising chain, *Phys. Rev. Lett.* **113**, 107204 (2014).
 - [5] S. Bera, H. Schomerus, F.H. Meisner, J.H. Bardarson, Many-body localization characterized from a one-particle perspective, *Phys. Rev. Lett.* **115**, 046603 (2015).
 - [6] L. Rademaker and M. Ortuño, Explicit local integrals of motion for the many-body localized state, *Phys. Rev. Lett.* **116**, 010404 (2016).
 - [7] V. Khemani, D. N. Sheng, and D. A. Huse, Two universality classes for the many-body localization transition, *Phys. Rev. Lett.* **119**, 075702 (2017).
 - [8] N. Maće, F. Alet, and N. Laflorencie, Multifractal scalings across the many-body localization transition, *Phys. Rev. Lett.* **123**, 180601 (2019).
 - [9] Y. Bar Lev, G. Cohen, and D. R. Reichman, Absence of diffusion in an interacting system of spinless fermions on a one-dimensional disordered lattice, *Phys. Rev. Lett.* **114**, 100601 (2015).
 - [10] E. Bairey, G. Refael, and N. H. Lindner, Driving induced many-body localization, *Phys. Rev. B* **96**, 020201(R) (2017).
 - [11] K. S. C. Decker, C. Karrasch, J. Eisert, and D. M. Kennes, Floquet Engineering Topological Many-Body Localized Systems, *Phys. Rev. Lett.* **124**, 190601 (2020).
 - [12] J. M. Deutsch, Eigenstate Thermalization Hypothesis, *Rep. Prog. Phys.* **81**, 082001 (2018).
 - [13] A. De Luca, A. Scardicchio, Ergodicity breaking in a model showing many-body localization, *Europhys. Lett.* **101**, 37003 (2013).
 - [14] Y. Bar Lev and D. R. Reichman, Dynamics of many-body localization, *Phys. Rev. B* **89**, 220201(R) (2014).
 - [15] D. J. Luitz, N. Laflorencie, and F. Alet, Extended slow dynamical regime close to the many-body localization transition, *Phys. Rev. B* **93**, 060201(R) (2016).
 - [16] D. A. Abanin, E. Altman, I. Bloch, and M. Serbyn, Colloquium: Many-body localization, thermalization, and entanglement, *Rev. Mod. Phys.* **91**, 021001 (2019).
 - [17] T. Guhr, A. Müller-Groeling, and H. A. Weidenmüller, Random-Matrix Theories in Quantum Physics: Common Concepts, *Phys. Rep.* **299**, 189 (1998).
 - [18] Y. Y. Atas, E. Bogomolny, O. Giraud, and G. Roux, Distribution of the Ratio of Consecutive Level Spacings in Random Matrix Ensembles, *Phys. Rev. Lett.* **110**, 084101 (2013).
 - [19] J. H. Bardarson, F. Pollmann, and J. E. Moore, Unbounded

- growth of entanglement in models of many-body localization, *Phys. Rev. Lett.* **109**, 017202 (2012).
- [20] M. Serbyn, Z. Papić, D.A. Abanin, Universal slow growth of entanglement in interacting strongly disordered systems, *Phys. Rev. Lett.* **110**, 260601 (2013).
- [21] B. Bauer and C. Nayak, Area Laws in a Many-Body Localized State and Its Implications for Topological Order, *J. Stat. Mech.* **2013**, P09005 (2013).
- [22] M. Serbyn, A. A. Michailidis, D. A. Abanin, and Z. Papić, Power-law entanglement spectrum in many-body localized phases, *Phys. Rev. Lett.* **117**, 160601 (2016).
- [23] Q. Guo, C. Cheng, Z.-H. Sun, Z. Song, H. Li, Z. Wang, W. Ren, H. Dong, D. Zheng, Y.-R. Zhang, R. Mondaini, H. Fan, and H. Wang, Observation of energy-resolved many-body localization, *Nat. Phys.* **17**, 234–239 (2021).
- [24] Q. Guo, C. Cheng, H. Li, S. Xu, P. Zhang, Z. Wang, C. Song, W. Liu, W. Ren, H. Dong, R. Mondaini, and H. Wang, Stark many-body localization on a superconducting quantum processor, *Phys. Rev. Lett.* **127**, 240502 (2021).
- [25] V. Ros, M. Müller, and A. Scardicchio, Integrals of Motion in the Many-Body Localized Phase, *Nucl. Phys. B* **891**, 420 (2015).
- [26] C. Bertoni, J. Eisert, A. Kshetrimayum, A. Nietner, and S. J. Thomson, Local Integrals of Motion and the Stability of Many-Body Localisation in Wannier-Stark Potentials [arXiv:2208.14432v4](https://arxiv.org/abs/2208.14432).
- [27] S. Gopalakrishnan, M. Müller, V. Khemani, M. Knap, E. Demler, D.A. Huse, Low-frequency conductivity in many-body localized systems, *Phys. Rev. B* **92**, 104202 (2015).
- [28] T. C. Berkelbach and D. R. Reichman, Conductivity of Disordered Quantum Lattice Models at Infinite Temperature: Many-Body Localization, *Phys. Rev. B* **81**, 224429 (2010).
- [29] A. Lazarides, A. Das, and R. Moessner, Fate of Many-Body Localization Under Periodic Driving, *Phys. Rev. Lett.* **115**, 030402 (2015).
- [30] L. D'Alessio and A. Polkovnikov, Many-Body Energy Localization Transition in Periodically Driven Systems, *Ann. Phys.* **333**, 19 (2013).
- [31] V. Khemani, A. Lazarides, R. Moessner, and S. L. Sondhi, Phase Structure of Driven Quantum Systems, *Phys. Rev. Lett.* **116**, 250401 (2016).
- [32] M. Schreiber, S. S. Hodgman, P. Bordia, H. P. Lüchen, M. H. Fischer, R. Vosk, E. Altman, U. Schneider, and I. Bloch, Observation of many-body localization of interacting fermions in a quasirandom optical lattice, *Science* **349**, 842 (2015).
- [33] P. Bordia, H. P. Lüchen, S. S. Hodgman, M. Schreiber, I. Bloch, and U. Schneider, Coupling Identical One-Dimensional Many-Body Localized Systems, *Phys. Rev. Lett.* **116**, 140401 (2016).
- [34] T. Kohlert, S. Scherg, X. Li, H. P. Lüchen, S. Das Sarma, I. Bloch, and M. Aidelsburger, Observation of Many-Body Localization in a One-Dimensional System with a Single-Particle Mobility Edge, *Phys. Rev. Lett.* **122**, 170403 (2019).
- [35] J. Smith, A. Lee, P. Richerme, B. Neyenhuis, P. W. Hess, P. Hauke, M. Heyl, D. A. Huse, and C. Monroe, Many-Body Localization in a Quantum Simulator with Programmable Random Disorder, *Nat. Phys.* **12**, 10 (2016).
- [36] P. Roushan et al., Spectroscopic Signatures of Localization with Interacting Photons in Superconducting Qubits, *Science* **358**, 1175 (2017).
- [37] N. F. Mott, Electrons in disordered structures, *Adv. Phys.* **16**, 49 (1967).
- [38] A. De Luca, B. L. Altshuler, V. E. Kravtsov, and A. Scardicchio, Anderson localization on the Bethe lattice: Nonergodicity of extended states, *Phys. Rev. Lett.* **113**, 046806 (2014).
- [39] W. De Roeck and F. Huveneers, Scenario for Delocalization in Translation-Invariant Systems, *Phys. Rev. B* **90**, 165137 (2014).
- [40] M. Brenes, M. Dalmonte, M. Heyl, and A. Scardicchio, Many-Body Localization Dynamics from Gauge Invariance, *Phys. Rev. Lett.* **120**, 030601 (2018).
- [41] G. H. Wannier, Dynamics of Band Electrons in Electric and Magnetic Fields, *Rev. Mod. Phys.* **34**, 645 (1962).
- [42] G. H. Wannier, Wave functions and effective hamiltonian for bloch electrons in an electric field, *Phys. Rev.* **117**, 432 (1960).
- [43] H. Fukuyama, R. A. Bari, and H. C. Foged by, Tightly bound electrons in a uniform electric field, *Phys. Rev. B* **8**, 5579 (1973).
- [44] E. van Nieuwenburg, Y. Baum, and G. Refael, From Bloch Oscillations to Many-Body Localization in Clean Interacting Systems, *Proc. Natl. Acad. Sci. USA* **116**, 9269 (2019).
- [45] M. Schulz, C. A. Hooley, R. Moessner, and F. Pollmann, Stark Many-Body Localization, *Phys. Rev. Lett.* **122**, 040606 (2019).
- [46] S. R. Taylor, M. Schulz, F. Pollmann, and R. Moessner, Experimental probes of Stark many-body localization, *Phys. Rev. B* **102**, 054206 (2020).
- [47] Y.-Y. Wang, Z.-H. Sun, and H. Fan, Stark Many-Body Localization Transitions in Superconducting Circuits, *Phys. Rev. B* **104**, 205122 (2021).
- [48] W. Morong, F. Liu, P. Becker, K. S. Collins, L. Feng, A. Kyprianidis, G. Pagano, T. You, A. V. Gorshkov, and C. Monroe, Observation of Stark Many-Body Localization without Disorder, *Nature* **599**, 393 (2021).
- [49] P. Ribeiro, A. Lazarides, and M. Haque, Many-Body Quantum Dynamics of Initially Trapped Systems Due to a Stark Potential: Thermalization Versus Bloch Oscillations, *Phys. Rev. Lett.* **124**, 110603 (2020).
- [50] R. Yao and J. Zakrzewski, Many-body localization of bosons in an optical lattice: Dynamics in disorder-free potentials, *Phys. Rev. B* **102**, 104203 (2020).
- [51] L. Zhang, Y. Ke, W. Liu, and C. Lee, Mobility Edge of Stark Many-Body Localization, *Phys. Rev. A* **103**, 023323 (2021).
- [52] T. M. Gunawardana and B. Buča, Dynamical L-Bits and Persistent Oscillations in Stark Many-Body Localization, *Phys. Rev. B* **106**, L161111 (2022).
- [53] X.-P. Jiang, R. Qi, S. Yang, Y. Hu, and G. Yang, Stark Many-Body Localization with Long-Range Interactions. [arxiv: 2307.12376v1](https://arxiv.org/abs/2307.12376).
- [54] C. M. Bender, Making Sense of Non-Hermitian Hamiltonians, *Rep. Prog. Phys.* **70**, 947 (2007).
- [55] Y. Ashida, Z. Gong, and M. Ueda, Non-Hermitian Physics, *Advances in Physics* **69**, 249 (2020).
- [56] K. Zhang, Z. Yang, and C. Fang, Correspondence between Winding Numbers and Skin Modes in Non-Hermitian Systems, *Phys. Rev. Lett.* **125**, 126402 (2020).
- [57] K. Zhang, Z. Yang, and C. Fang, Universal Non-Hermitian Skin Effect in Two and Higher Dimensions, *Nat. Commun.* **13**, 2496 (2022).
- [58] Z. Ou, Y. Wang, and L. Li, Non-Hermitian Boundary Spectral Winding, *Phys. Rev. B* **107**, L161404 (2023).
- [59] S. Yao and Z. Wang, Edge States and Topological Invariants of Non-Hermitian Systems, *Phys. Rev. Lett.* **121**, 086803 (2018).
- [60] D. S. Borgnia, A. J. Kruchkov, and R.-J. Slager, Non-Hermitian Boundary Modes and Topology, *Phys. Rev. Lett.* **124**, 056802 (2020).
- [61] K. Yokomizo and S. Murakami, Non-Bloch Band Theory of Non-Hermitian Systems, *Phys. Rev. Lett.* **123**, 066404 (2019).
- [62] Y.-C. Wang, J.-S. You, and H. H. Jen, A non-Hermitian optical atomic mirror, *Nat. Commun.* **13**, 4598 (2022).
- [63] Zhihao Xu, Shu Chen, Topological Bose-Mott insulators in

- one-dimensional non-Hermitian superlattices, *Phys. Rev. B* **102**, 035153 (2020).
- [64] R. Hamazaki, K. Kawabata, N. Kura, and M. Ueda, Universality Classes of Non-Hermitian Random Matrices, *Phys. Rev. Research* **2**, 023286 (2020).
- [65] Lucas Sá, Pedro Ribeiro, and Tomaž Prosen, Complex Spacing Ratios: A Signature of Dissipative Quantum Chaos, *Phys. Rev. X* **10**, 021019 (2020).
- [66] A. M. García-García, L. Sá, and J. J. M. Verbaarschot, Symmetry Classification and Universality in Non-Hermitian Many-Body Quantum Chaos by the Sachdev-Ye-Kitaev Model, *Phys. Rev. X* **12**, 021040 (2022).
- [67] J. Ginibre, Statistical Ensembles of Complex, Quaternion, and Real Matrices, *J. Math. Phys.* **6**, 440 (1965).
- [68] N. Hatano and D. R. Nelson, Localization Transitions in Non-Hermitian Quantum Mechanics, *Phys. Rev. Lett.* **77**, 570 (1996).
- [69] N. Hatano and D. R. Nelson, Vortex Pinning and Non-Hermitian Quantum Mechanics, *Phys. Rev. B* **56**, 8651 (1997).
- [70] N. Hatano and D. R. Nelson, Non-Hermitian Delocalization and Eigenfunctions, *Phys. Rev. B* **58**, 8384 (1998).
- [71] R. Hamazaki, K. Kawabata, and M. Ueda, Non-Hermitian Many-Body Localization, *Phys. Rev. Lett.* **123**, 090603 (2019).
- [72] L.-Z. Tang, G.-Q. Zhang, L.-F. Zhang, and D.-W. Zhang, Localization and topological transitions in non-Hermitian quasiperiodic lattices, *Phys. Rev. A* **103**, 033325 (2021).
- [73] L.-J. Zhai, S. Yin, and G.-Y. Huang, Many-body localization in a non-Hermitian quasiperiodic system, *Phys. Rev. B* **102**, 064206 (2020).
- [74] Z. Gong, Y. Ashida, K. Kawabata, K. Takasan, S. Higashikawa, and M. Ueda, Topological Phases of Non-Hermitian Systems, *Phys. Rev. X* **8**, 031079 (2018).
- [75] Q. Lin, T. Li, L. Xiao, K. Wang, W. Yi, and P. Xue, Topological Phase Transitions and Mobility Edges in Non-Hermitian Quasicrystals, *Phys. Rev. Lett.* **129**, 113601 (2022).
- [76] S. Weidemann, M. Kremer, S. Longhi, and A. Szameit, Topological Triple Phase Transition in Non-Hermitian Floquet Quasicrystals, *Nature (London)* **601**, 354 (2022).
- [77] J. Dalibard, Y. Castin, and K. Mømer, Wave-Function Approach to Dissipative Processes in Quantum Optics, *Phys. Rev. Lett.* **68**, 580 (1992).
- [78] M. Nakagawa, N. Tsuji, N. Kawakami, and M. Ueda, Dynamical Sign Reversal of Magnetic Correlations in Dissipative Hubbard Models, *Phys. Rev. Lett.* **124**, 147203 (2020).
- [79] T. E. Lee and C.-K. Chan, Heralded Magnetism in Non-Hermitian Atomic Systems, *Phys. Rev. X* **4**, 041001 (2014).
- [80] E. Levi, M. Heyl, I. Lesanovsky, and J. P. Garrahan, Robustness of many-body localization in the presence of dissipation, *Phys. Rev. Lett.* **116**, 237203 (2016).
- [81] K. Suthar, Y.-C. Wang, Y.-P. Huang, H. H. Jen, and J.-S. You, Non-Hermitian many-body localization with open boundaries, *Phys. Rev. B* **106**, 064208 (2022).
- [82] S. Longhi, Topological Phase Transition in Non-Hermitian Quasicrystals, *Phys. Rev. Lett.* **122**, 237601 (2019).
- [83] M. Arikawa, I. Maruyama, and Y. Hatsugai, *Phys. Rev. B* **82**, 073105 (2010).
- [84] S. Ghosh, S. Gupta, and M. Kulkarni, Spectral Properties of Disordered Interacting Non-Hermitian Systems, *Phys. Rev. B* **106**, 134202 (2022).
- [85] T. Peron, B. M. F. De Resende, F. A. Rodrigues, L. D. F. Costa, and J. A. Méndez-Bermúdez, Spacing Ratio Characterization of the Spectra of Directed Random Networks, *Phys. Rev. E* **102**, 062305 (2020).
- [86] T. Orito and K.-I. Imura, Unusual wave-packet spreading and entanglement dynamics in non-Hermitian disordered many-body systems, *Phys. Rev. B* **105**, 024303 (2022).
- [87] N. Hatano and H. Obuse, Delocalization of a Non-Hermitian Quantum Walk on Random Media in One Dimension, *Ann. Phys.* **435**, 168615 (2021).
- [88] F. Alsallom, L. Herviou, O. V. Yazyev, and M. Brzezińska, Fate of the Non-Hermitian Skin Effect in Many-Body Fermionic Systems, *Phys. Rev. Research* **4**, 033122 (2022).
- [89] W. Gou, T. Chen, D. Xie, T. Xiao, T.-S. Deng, B. Gadway, W. Yi, and B. Yan, Tunable Nonreciprocal Quantum Transport through a Dissipative Aharonov-Bohm Ring in Ultracold Atoms, *Phys. Rev. Lett.* **124**, 070402 (2020).
- [90] Q. Liang, D. Xie, Z. Dong, H. Li, H. Li, B. Gadway, W. Yi, and B. Yan, Dynamic Signatures of Non-Hermitian Skin Effect and Topology in Ultracold Atoms, *Phys. Rev. Lett.* **129**, 070401 (2022).
- [91] H.-Z. Li, X.-J. Yu, and J.-X. Zhong, Non-Hermitian Stark Many-Body Localization. *arXiv:2305.09387v1*